Simultaneous Segmentation of Multiple Closed Surfaces Using Optimal Graph Searching

Kang Li[1], Steven Millington[2], Xiaodong Wu[3],
Danny Z. Chen[4], and Milan Sonka[3]

[1] Dept. of Electrical and Computer Engineering, Carnegie Mellon University,
5000 Forbes Ave, Pittsburgh, PA 15213, USA
kangl@cmu.edu
[2] Frank Stronach Institute, Infeldgasse 21B/II, A8010 Graz, Austria
steven.millington@tugraz.at
[3] Dept. of Electrical and Computer Engineering, The University of Iowa,
4016 Seamans Center, Iowa City, IA 52242-1595, USA
{xiaodong-wu, milan-sonka}@uiowa.edu
[4] Dept. of Computer Science and Engineering, The University of Notre Dame
Notre Dame, IN 46556, USA
dchen@cse.nd.edu

Abstract. This paper presents a general graph-theoretic technique for simultaneously segmenting multiple closed surfaces in volumetric images, which employs a novel graph-construction scheme based on triangulated surface meshes obtained from a topological presegmentation. The method utilizes an efficient graph-cut algorithm that guarantees global optimality of the solution under given cost functions and geometric constraints. The method's applicability to difficult biomedical image analysis problems was demonstrated in a case study of co-segmenting the bone and cartilage surfaces in 3-D magnetic resonance (MR) images of human ankles. The results of our automated segmentation were validated against manual tracings in 55 randomly selected image slices. Highly accurate segmentation results were obtained, with signed surface positioning errors for the bone and cartilage surfaces being 0.02 ± 0.11mm and 0.17 ± 0.12mm, respectively.

1 Introduction

Optimal segmentation of surfaces representing object boundaries in volumetric datasets is important and challenging for many medical image analysis applications. Recently, we proposed an efficient algorithm for d-D ($d \geq 3$) optimal hyper-surface detection with hard smoothness constraints, making globally optimal surface segmentation in volumetric images practical [1, 2]. By modeling the problem with a *geometric graph*, the method transforms the segmentation problem into computing the minimum s-t graph cut that is well-studied in graph theory, and makes the problem solvable in a low-order polynomial time. The solution is guaranteed to be globally optimal in the considered region by theoretical

G.E. Christensen and M. Sonka (Eds.): IPMI 2005, LNCS 3565, pp. 406–417, 2005.
© Springer-Verlag Berlin Heidelberg 2005

(a) Coronal view (b) Sagittal view

Fig. 1. Two sample slices of a 3-D MR image of human ankle

proofs [1]. We have also developed a multi-surface segmentation algorithm [3]. However, these methods were both limited to segmenting height-field or cylindrical surfaces in regular grids.

In this paper, we present a non-trivial extension of our previous work. We focus on the problem of segmenting *optimal multiple closed* surfaces in 3-D. The new method for multiple surfaces segmentation is motivated by the need to accurately segment cartilage layers in diseased joints. In this application, the articular cartilage and corresponding subchondral bone surfaces can be imaged by 3-D high-resolution MRI (Fig. 1). However, no segmentation method exists that would allow a rapid, accurate, and reproducible segmentation for quantitative evaluation of articular cartilage.

The main contribution of our work is that it extends the optimal graph-searching techniques to closed surfaces, while the backbone of our approach – graph-cuts – is radically different from traditional graph searching. Consequently, many existing problems that were tackled using graph-searching in a slice-by-slice manner can be migrated to our new framework with little or no change to the underlying objective function formulation.

2 Methods

The proposed method allows segmenting multiple inter-related surfaces in volumetric images and facilitates subsequent quantitative analysis. We will utilize the bone–cartilage segmentation task to help make the method description intuitively clear. The general strategy of our method is to achieve the final segmentation in two stages. The initial stage provides approximate segmentation of the three-dimensional object (in our case, of the bone), and the final segmentation is achieved by accurate and simultaneous segmentation of its multiple surfaces

of interest. The outputs of the algorithm are triangulated meshes that are ready for visualization and quantitative measurement.

The method consists of the following three main steps:

1. *Bone surface presegmentation.* A level set based algorithm is used. Starting from several seed-spheres, the method uses the image-derived edge and regional information to evolve a smooth surface toward the bone boundary. The presegmented surface serves as an initialization to the subsequent segmentation.
2. *Mesh generation and optimization.* The presegmentation results in an implicit surface that is the zero level set of a 4-D function embedded in a volumetric digital grid. An isosurfacing algorithm (e.g., marching cubes) is used to convert the implicit surface into an explicit triangulated mesh. The mesh is optimized by removing or merging isolated and redundant triangles. The resolution of the mesh can be increased or decreased using progressive level of detail approaches when necessary.
3. *Co-segmentation of the cartilage and bone surfaces.* The mesh generated by the second step is used to initialize a graph in a narrow-band around the presegmented bone surface. A novel multi-surfaces graph search algorithm is used to simultaneously obtain the precise positions of the bone and cartilage surfaces based on two cost functions separately designed for the two surfaces while considering specific geometric constraints.

Since the mesh manipulation step involves largely standard techniques in graphics, only the first and third steps are described in detail.

2.1 Bone Surface Presegmentation

The presegmentation algorithm is based on the *MetaMorphs* deformable shape and texture model presented in [4]. The method provides a unified gradient-descent framework for modeling both the boundary and texture information in an image, and is relatively efficient in computation.

Let Ω denote the image domain, and $\partial\Omega$ be the surface represented by the model, which is the zero level set of a signed distance function ϕ. ϕ is positive in the model interior, denoted Ω^+. Instead of directly evolving the function ϕ, the deformation of the surface is controlled by a set of uniformly-spaced control points artificially embedded in the image domain. The motion of the control points is computed using image-derived information. The deformation at any voxel location can then be derived using the cubic B-spline based Free Form Deformation (FFD). As such, the level set function ϕ can be updated using a geometric transformation of itself at each descent step. The motion of the control points is determined by minimizing the weighted combination of two edge-based cost terms and two region-based cost terms. For more detail of the cost terms and the model evolution, we refer to reader to [4].

Particularly, in [4], the authors suggested a Gaussian kernel-based nonparametric approach for modeling image pixel (voxel) intensity distributions. This approach, however, is computationally expensive in 3-D. Considering our

application domain and taking advantage of the physical properties of the MR images, voxel intensities in the bone region are approximated by a Rayleigh distribution:

$$P(I|b) = \frac{Ie^{-I^2/2b^2}}{b^2}, \quad I \geq 0, \;\; b > 0 \tag{1}$$

with I being the pixel intensity. This distribution has only one free parameter b, which is estimated using the sample mean μ of voxel intensities inside the initializing spheres, as:

$$b = \mu\sqrt{\frac{2}{\pi}} \tag{2}$$

2.2 Simultaneous Segmentation of Cartilage and Bone Surfaces

After the bone surface is presegmented and converted into a triangulated mesh, a novel graph-based algorithm is applied to co-optimize the cartilage and bone surfaces. Note that anatomically, the cartilage only covers certain parts of the bone surface. To simplify the problem, we assume the cartilage extends the full surface area of the bone. However, in some areas the "cartilage" surface merges with the bone, so that the cartilage thickness is effectively zero in those areas.

Preliminaries. A triangulated mesh consists of a set of *vertices* connected by *edges*. We use $\mathcal{M}(\mathcal{V}, \mathcal{E})$ to denote a mesh with vertex set $\mathcal{V}$ and edge set $\mathcal{E}$. Two vertices are said to be *adjacent* if they are connected by an edge. Each vertex has an associated surface *normal*, which is perpendicular to the surface that the mesh represents at the vertex.

A graph $\mathcal{G}(\mathcal{N}, \mathcal{A})$ is a structure that consists of a set of *nodes* $\mathcal{N}$ and a set of *arcs* $\mathcal{A}$. The arc connecting two nodes n_1 and n_2 is denoted by $\langle n_1, n_2\rangle$. For *undirected* arcs, the notations $\langle n_1, n_2\rangle$ and $\langle n_2, n_1\rangle$ are considered equivalent. For a *directed* arc, they are considered distinct. The former one denotes the arc from n_1 to n_2, and the latter one from n_2 to n_1. In addition, a *geometric* graph is a graph whose nodes have certain geometric positions in space.

Graph Construction. Since the bone and cartilage surfaces are to be segmented simultaneously, two spatially-coincident *columns* of equidistant nodes are constructed along the normal at each vertex of the triangular mesh obtained from the presegmentation (Fig. 2). The number of nodes in each column is determined by the required resolution, and the extent of each column depends on the width of the region where the cartilage and bone surfaces are expected – a narrow-band around the presegmented surface. A set of arcs is carefully constructed between the nodes to ensure the geometric constraints, including the *smoothness constraint*, which controls the stiffness of the output surfaces, and the surface *separation constraint*, which defines the relative positioning and the distance range of the two surfaces.

Suppose there are N vertices on the mesh, and let v_i be one of them ($i \in \{0, \ldots, N-1\}$). The two columns of nodes constructed along the normal at v_i are denoted by $\mathcal{K}_0(v_i) \equiv \{n_{0i}^0, \ldots, n_{0i}^{K-1}\}$ and $\mathcal{K}_1(v_i) \equiv \{n_{1i}^0, \ldots, n_{1i}^{K-1}\}$,

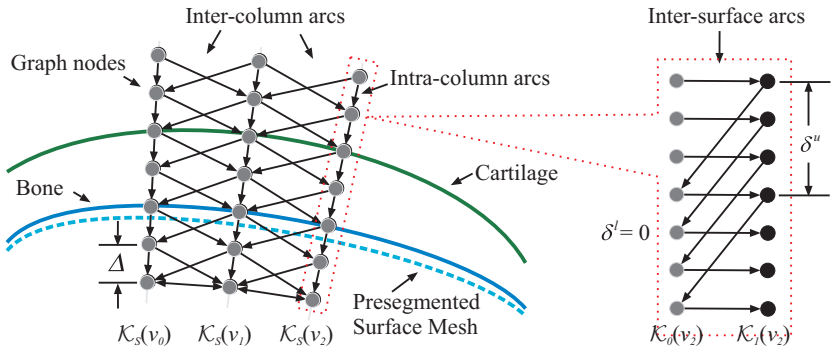

Fig. 2. Graph construction

respectively, where K is the number of nodes in each column. The collection of columns $\bigcup \mathcal{K}_s(v_i)$ with $s = 0, 1$ and $i = 1, \ldots, N-1$ constitutes the node set $\mathcal{N}$.

Next, assuming that each column $\mathcal{K}_0(v_i)$ intersects with the bone surface at exactly one node, denoted n^*_{0i}, and each column $\mathcal{K}_1(v_i)$ intersects with the cartilage surface at exactly one node n^*_{1i}, the collections of nodes $\mathcal{N}^*_0 \equiv \{n^*_{0i} : i = 0, \ldots, N-1\}$ and $\mathcal{N}^*_1 \equiv \{n^*_{1i} : i = 0, \ldots, N-1\}$ will represent discretizations of the bone surface and the cartilage surface, respectively. In this way, the segmentation problem is converted to a graph search problem, in which the node sets $\mathcal{N}^*_0$ and $\mathcal{N}^1_1$ are to be identified.

Apparently, the choices of $\mathcal{N}^*_0$ and $\mathcal{N}^*_1$ are not arbitrary. Cost values are assigned to the graph nodes according to two cost functions constructed specifically for the bone and cartilage surfaces. $\mathcal{N}^*_0$ and $\mathcal{N}^*_1$ will correspond to the set of nodes with the minimum total cost in the graph. Furthermore, several constraints are imposed on the geometric relations of the nodes in $\mathcal{N}^*_0$ and $\mathcal{N}^*_1$. These constraints are enforced by the graph arcs, constructed as follow.

- *Intra-column arcs* $\mathcal{A}^a$: Along each column $\mathcal{K}_s(v_i)$, every node n^k_{si} has a directed arc to the node n^{k-1}_{si}, i.e.,

$$\mathcal{A}^a = \{\langle n^k_{si}, n^{k-1}_{si}\rangle : k = 1, \ldots, K-1; \forall i, s\} \tag{3}$$

- *Inter-column arcs* $\mathcal{A}^r$: The inter-column arcs encode the smoothness constraint, which is imposed between each pair of adjacent columns. Two columns $\mathcal{K}_s(v_i)$ and $\mathcal{K}_s(v_j)$ ($s \in \{0, 1\}$, $i \neq j$) are said to be adjacent if the two vertices v_i and v_j are adjacent on the mesh. Suppose one of the sought surfaces intersects with two adjacent columns $\mathcal{K}_s(v_i)$ and $\mathcal{K}_s(v_j)$ at nodes $n^{k_i}_{si}$ and $n^{k_j}_{sj}$, respectively. If the surface is smooth, k_i and k_j should not differ too much. The smoothness constraint Δ defines the maximum allowed difference between k_i and k_j, i.e., $\Delta = \max |k_i - k_j|$. Smaller Δ forces the surface to be smoother. To encode the smoothness constraint in the graph, the following directed arcs are constructed:

$$\mathcal{A}^r = \{\langle n^k_{si}, n^{\max(0,k-\Delta)}_{sj}\rangle : \forall s, k;\ v_i, v_j \text{ adjacent}\} \tag{4}$$

– *Inter-surface arcs* $\mathcal{A}^s$: These arcs model the separation constraint between the two surfaces. Suppose the bone and cartilage surfaces intersect $\mathcal{K}_0(v_i)$ and $\mathcal{K}_1(v_i)$ at nodes $n_{0i}^{k_0}$ and $n_{1i}^{k_1}$, respectively. Because the thickness of the cartilage is within some known range, $n_{0i}^{k_0}$ and $n_{1i}^{k_1}$ are at least δ^l, and at most δ^u nodes apart, i.e., $\delta^l \leq k_1 - k_0 \leq \delta^u$. The inter-surface arcs are constructed between columns $\mathcal{K}_0(v_i)$ and $\mathcal{K}_1(v_i)$ for all $v_i \in \mathcal{V}$ as:

$$\mathcal{A}^s = \{\langle n_{1i}^k, n_{0i}^{\max(0,k-\delta^u)}\rangle, \langle n_{0i}^k, n_{1i}^{\min(K-1,k+\delta^l)}\rangle : \forall i, k\} \tag{5}$$

For more than two surfaces, the separation constraint is specified pairwisely.

Cost Functions. The cost functions are crucial for accurate surface localization. For this pilot study, relatively simple cost functions are used. Specifically, the cost function for the bone surface, C_{bone}, is the negated gradient magnitude of the Gaussian-smoothed image G,

$$C_{bone} = -|\nabla G| \equiv -\sqrt{G_x^2 + G_y^2 + G_z^2} \tag{6}$$

where $G_x \equiv \frac{\partial}{\partial x}G$, $G_y \equiv \frac{\partial}{\partial y}G$ and $G_z \equiv \frac{\partial}{\partial z}G$ are partial derivatives of the image. The cost function for the cartilage surface is computed as a weighted combination of the response of a 3-D "sheet filter" [5] and the directional image gradients. The sheet filter is formulated using the Hessian matrix $\nabla^2 G$ of the image intensity. Let the eigenvalues of $\nabla^2 G$ be λ_0, λ_1 and λ_2, $(\lambda_0 \geq \lambda_1 \geq \lambda_2)$. The sheet filter is defined as:

$$F_{sheet}(G) = \begin{cases} |\lambda_2| \cdot \omega(\lambda_1, \lambda_2) \cdot \omega(\lambda_0, \lambda_2), & \lambda_2 < 0, \\ 0, & \text{otherwise.} \end{cases} \tag{7}$$

The function ω is given by:

$$\omega(\lambda_a, \lambda_b) = \begin{cases} (1 + \frac{\lambda_a}{|\lambda_b|})^\gamma, & \lambda_b \leq \lambda_a \leq 0, \\ (1 - \alpha\frac{\lambda_a}{|\lambda_b|})^\gamma, & \frac{|\lambda_b|}{\alpha} > \lambda_a > 0, \\ 0, & \text{otherwise,} \end{cases} \tag{8}$$

where α, γ are parameters. In our experiments, we chose $\alpha = 0.25$ and $\gamma = 0.5$.

In summary, the cost function for cartilage surface is computed as:

$$C_{cartilage} = \begin{cases} -F_{sheet}(-G) - \tau_x G_x, & \text{if } G_x > 0, \\ -F_{sheet}(-G) & \text{otherwise,} \end{cases} \tag{9}$$

where the value of τ_x is chosen to be 1.0 in our experiments.

The above cost functions are computed in the image domain. The node costs are assigned using spatial interpolation based on the positions of the nodes. Specifically, the costs of nodes n_{0i}^k are assigned according to C_{bone}, and the costs of nodes n_{1i}^k are computed from $C_{cartilage}$.

Optimization. Once the graph is constructed and the node costs assigned, we can use the same technique described in [3] to transform the graph into an s-t graph $\mathcal{G}_{st}$ that has a source node s and a sink node t, and apply a minimum s-t cut algorithm to compute the optimal surfaces. The final surfaces will correspond to the upper envelope of the set of nodes that can be reached from s in $\mathcal{G}_{st}$, i.e., the source set of $\mathcal{G}_{st}$.

3 Case Study

Osteoarthritis and articular cartilage injuries are very common – one in six people in the USA is affected by some form of arthritis. The socio-economic impact of degenerative joint diseases is massive, with an estimated annual cost of $65 billion in the USA during the 1990's. As such, there is a huge research interest in the field of chondro-protective and chondro-restorative treatments.

The proposed method allows segmenting the articular cartilage surface and the corresponding subchondral bone surface in volumetric MRI images that facilitates subsequent quantitative analysis. The segmentation is initiated by a few (normally 3 or less) roughly-placed seed points in the bone region, but is otherwise fully automated.

Data. The method was tested in 8 high-resolution 3-D MR data sets of human ankles. The images were acquired using a 1.5T MR scanner, with in plane resolution 0.3×0.3 mm^2 and slice thickness 0.3 mm. The acquisition time was 17 minutes and 14 seconds. Overall, each MR image data set consisted of approximately $512 \times 512 \times 150$ voxels.

Independent Standard. In the 8 MR images, 55 coronal or sagittal slices were randomly selected to be manually traced by an expert observer (orthopedic surgeon) and formed the independent standard. The selection of coronal as well as sagittal slices allows assessing the performance of the inherently 3-D segmentation method using 2-D manual tracings.

Comparisons with the Independent Standard. Computer segmentation of the talus bone and the cartilage surfaces was performed in 3-D. Consequently, the segmented surfaces were available for the entire closed 3-D object. The automated segmentation method locally failed in 5 of the 55 image slices for which independent standard was available due to local pre-segmentation errors. The segmentation accuracy was assessed in the 50 image slices by computing signed, unsigned, and RMS surface positioning errors. The positioning errors were defined as the shortest distances between the manually traced borders and the computer-determined surfaces in the coronal and sagittal MR slices for which the independent standard was available. The errors are reported on a per-slice basis as mean $\pm$ standard deviation.

Reproducibility. To assess the reproducibility of cartilage segmentation, the method was independently initialized 5 times and the mean and maximum car-

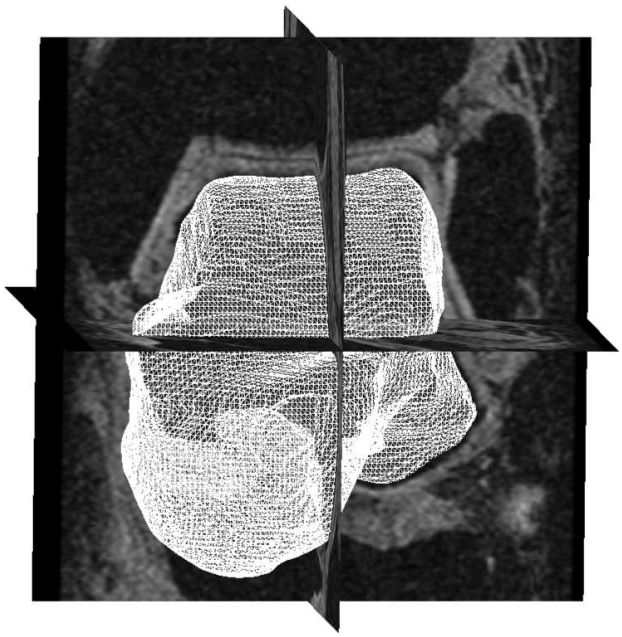

(a) Presegmented talus surface

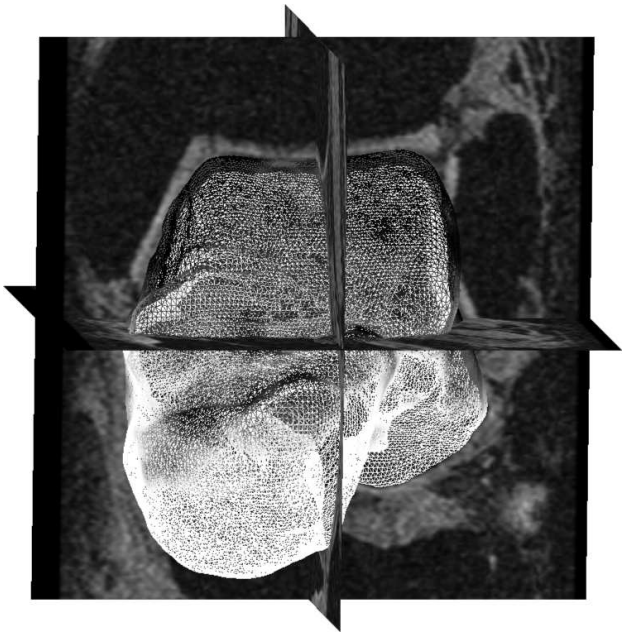

(b) Segmented talus and cartilage

Fig. 3. Presegmentation and segmentation. Cartilage surfaces are color-coded, with darker shadings depicting thicker cartilage

tilage thicknesses were determined for each of the 8 talus cartilages. The reproducibility was assessed by calculating mean ± standard deviation of differences between the average values obtained in the 5 reproducibility runs and the individual results.

Results. All experiments were performed on a workstation with dual 3.0GHz processors and 4GB of RAM. For each data set, we used 3 seed-spheres inside the

Table 1. Overall surface positioning accuracy

	Signed Error (mm)	Unsigned Error (mm)	RMS Error (mm)
Bone	0.02 ± 0.11	0.25 ± 0.08	0.03 ± 0.01
Cartilage	0.17 ± 0.12	0.39 ± 0.09	0.04 ± 0.01

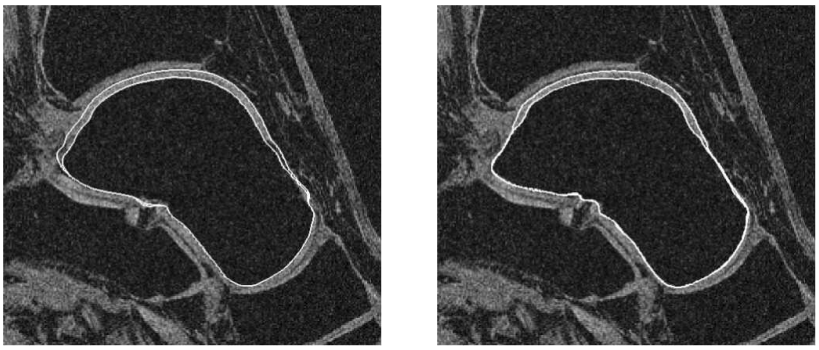

(a) Computer (b) Manual

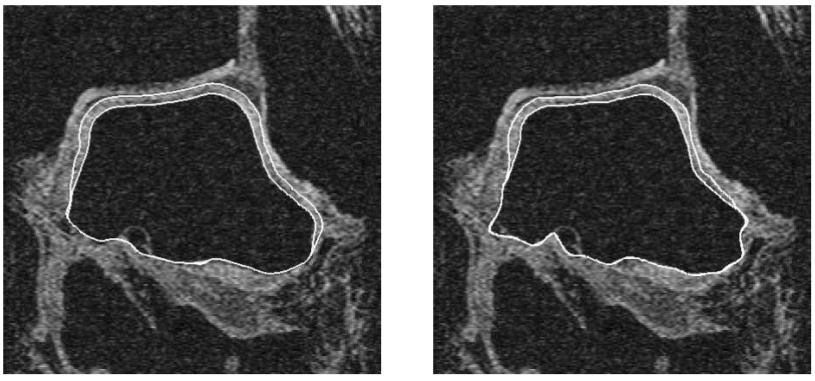

(c) Computer (d) Manual

Fig. 4. Comparison of computer and manual segmentations

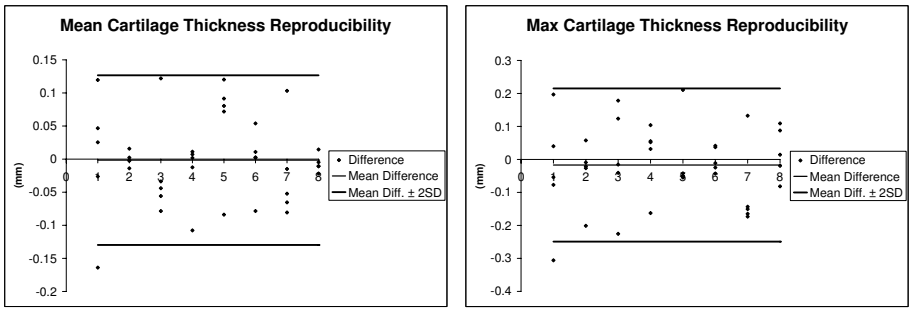

(a) Mean cartilage thickness (b) Max cartilage thickness

Fig. 5. Bland-Altman plots of cartilage thickness reproducibility

bone region to initialize the presegmentation. To reduce running time, the regions containing the talus bones were cropped from the original MR images to form smaller images of approximately 250×250×150 voxels each. The presegmentation was performed on 2-times downsampled copies of the cropped images, while the final segmentation was performed on the original full-resolution images.

The parameters used for final segmentations were $K = 30$, $\delta^l = 0$, $\delta^u = 12$ and $\Delta = 1$. For each data set, the average execution times of the presegmentation and segmentation stages were about 200 seconds and 70 seconds, respectively. The overall surface positioning errors of the computer-segmented talus bone and its cartilage surfaces are shown in Table 1. Examples of computer-segmented and manually-traced bone and cartilage contours are shown in Fig. 4.

The mean cartilage thickness measurements achieved a signed error of 0.08 ± 0.07mm, and an unsigned error of 0.09 ± 0.06mm. The corresponding measurements of maximum cartilage thicknesses have signed and unsigned errors of 0.01 ± 0.19mm and 0.16 ± 0.10mm, respectively. All border positioning errors show subvoxel accuracy (voxel size $0.3 \times 0.3 \times 0.3$ mm^3).

In the reproducibility experiment, the initializing spheres were modified from the original settings by adding up to 10% of random perturbations to their radii and 2 to 5 voxels of random translations to each coordinate of their positions. The Bland-Altman plots of the signed differences between each individual measurement and the average measurements are shown in Fig. 5 demonstrating that repeated measurement of cartilage thickness is unbiased and reproducible.

4 Discussion and Conclusion

Traditional techniques such as manual segmentation and gradient based edge detection are not suitable for automated, accurate, reproducible detection of the cartilage and subchondral bone surfaces in thin congruent cartilage layers. The objective of this study was to provide a proof of concept that the cartilage

and subchondral bone surfaces can be accurately detected simultaneously in 3-D, using a novel segmentation method, and perform its pilot validation in comparison with an independent standard.

Properties of the Method. The graph-based segmentations utilized hard geometric constraints, which are intuitive and easily controllable. The definition of the smoothness constraint, however, requires that the edges in the surface mesh be as equidistant as possible. This could be achieved by using sophisticated mesh optimization algorithms. An alternative and simpler way is to make the smoothness constraint vary between graph columns by modulating it according to the corresponding edge length. When the mesh is dense enough, however, the effect of unequal edge length could be ignored for our application. Therefore, neither approach was used in the reported experiments. A drawback of the presented graph-search approach is its dependence on presegmentation, which is crucial for obtaining good final results. However, a one-shot approach using either numerical or discrete mathematical tools alone could be difficult to design, computationally inefficient and may not yield a satisfactory outcome. In addition, its reliance on surface normals makes the method suffer from surface self-intersections. However, this problem is avoidable by detecting spatially intersecting node columns and pruning the affected nodes during the graph-construction.

The employed presegmentation method uses free form deformation, with which one can use large step size for surface evolution. Moreover, in practice, the number of control points required for the FFD is usually much fewer than the number of image voxels. These make the method computationally efficient.

Overall, the method was shown to be highly reproducible in our experiments. However, the initialization of the presegmentation is quite strategic. As a rule of thumb, the seed-spheres should be roughly centered at the maxima of the "shape image" in the bone interior. Automatic initialization methods can be designed following this strategy.

Cartilage Segmentation. A variety of 2-D image segmentation techniques have been utilized on articular cartilage images in the past, including manual segmentation, seed point and region growing algorithms, fully automated 2-D shape recognition, interpolated B-splines, B-spline snakes, and directional gradient vector flow snakes [6, 7, 8]. All of these techniques have limitations as they require an accurate initialization. Manual surface segmentation is both labor intensive and prone to error and is influenced by subjective judgment of the operator leading to inter-observer variability. Moreover, the accuracy and reproducibility of existing fully automated and semi-automated algorithms in noisy images of cartilage layers are often suboptimal. This poses particular problems in thin highly congruent, curved cartilage layers, which require subvoxel measurement accuracy. Previous studies utilizing computer-assisted techniques suffer from measurement errors of up to 100% or exclude large areas of the joint surface. As a result there has been a return to manual segmentation techniques with the focus being on the development of time saving devices such as touch screen interactive segmentation. The reported 3-D approach addresses a number

of the existing challenges and carries a substantial promise for the future utility of automated quantitative analysis of cartilage in 3-D.

Conclusion. A novel method for simultaneously segmenting multiple closed surfaces was demonstrated. The method utilizes an efficient graph-based algorithm that produces optimal solutions according to certain cost functions and geometric constraints. The proposed method achieved highly accurate results in segmenting cartilage and bone surfaces in MR images of human ankles. Although this paper concentrated on closed surfaces, the presented method can segment surfaces of other topologies according to different initializing meshes.

References

1. X. Wu and D. Z. Chen, "Optimal net surface problems with applications," in *Proc. of the 29th International Colloquium on Automata, Languages and Programming (ICALP)*, July 2002, pp. 1029–1042.
2. K. Li, X. Wu, D. Z. Chen, and M. Sonka, "Efficient optimal surface detection: Theory, implementation and experimental validation," in *Proc. SPIE International Symposium on Medical Imaging: Image Processing*, vol. 5370, May 2004, pp. 620–627.
3. ——, "Globally optimal segmentation of interacting surfaces with geometric constraints," in *Proc. IEEE Computer Society Conference on Computer Vision and Pattern Recognition (CVPR)*, vol. I, June 2004, pp. 394–399.
4. X. Huang, D. Metaxas, and T. Chen, "Metamorphs: Deformable shape and texture models," in *Proc. IEEE Computer Society Conference on Computer Vision and Pattern Recognition (CVPR)*, vol. I, June 2004, pp. 496–503.
5. Y. Sato, C.-F. Westin, A. Bhalerao, S. Nakajima, N. Shiraga, S. Tamura, and R. Kikinis, "Tissue classification based on 3D local intensity structure for volume rendering," *IEEE Trans on Visualization and Computer Graphics*, vol. 6, no. 2, pp. 160–180, 2000.
6. C. G. Peterfy, C. F. van Dijke, D. L. Janzen, C. C. Gluer, R. Namba, S. Majumdar, P. Lang, and H. K. Genant, "Quantification of articular cartilage in the knee with pulsed saturation transfer subtraction and fat-suppressed MR imaging: optimization and validation," *Radiology*, vol. 192, pp. 485–491, 1994.
7. A. Stammberger, F. Eckstein, M. Michaelis, K. H. Englmeier, and M. Reiser, "Interobserver reproducibility of quantitative cartilage measurement: comparison between B-spline snakes and manual segmentation," *Magnetic Resonance Imaging*, vol. 17, pp. 1033–1042, 1999.
8. J. Tang, S. Millington, S. Acton, J. Crandall, and S. Hurwitz, "Cartilage surface tracking using directional gradient vector flow snakes," in *IEEE Int. Conf. on Image Processing*, Singapore, 2004.